Desalination and Water Treatment
www.deswater.com
doi: 10.5004/dwt.2023.30154

316 (2023) 91–110
December

Experimental and computational study on the anti-re-entrainment performance of an innovative demister with embedded drainage channels

Shi Bu[a,b,*], Yong Jia[a], Quan Yang[a], Zhengjun Yang[a], Meilian Yang[a]

[a]*School of Mechanical Engineering and Rail Transit, Changzhou University, Changzhou 213164, China, emails: bushi@cczu.edu.cn (S. Bu), 2814887969@qq.com (Y. Jia), yangquan_douglas@qq.com (Q. Yang), 1064765798@qq.com (Z. Yang), 1186462120@qq.com (M. Yang)*
[b]*Jiangsu Key Laboratory of Green Process Equipment, Changzhou 213164, China*

Received 1 August 2023; Accepted 20 November 2023

ABSTRACT

An innovative demister design with embedded drainage channels is proposed for the purpose of achieving higher anti-re-entrainment performance in multi-stage flash (MSF) desalination applications. Experimental work producing ultra fine droplets (≤50 μm) is carried out to systematically assess the influence of plate interval (22–30 mm) and inlet velocity upon pressure loss and separation efficiency. Numerical simulation employing turbulence SST *k*–ω model and Euler-Wall-Film model is conducted to study the flow field details in the demister passage. The results indicate that the critical inlet velocity can be improved to 8.5 m/s which yields excellent anti-re-entrainment ability and hence higher treating capacity of MSF. The embedded drainage channels act an essential role in resisting secondary droplets, suppressing shear force and enhancing liquid collection through integrated design and vortex generation. The new demister especially receives outstanding comprehensive performance at higher inlet velocities thanks to its stronger anti-re-entrainment ability. Despite the trade-off between overall separation efficiency and anti-re-entrainment, an overall better performance can be achieved with the new type if compared to the conventional designs. The superiority of the proposed innovative demisters with embedded drainage channels is also revealed by higher withstood maximum velocity, indicating potential to improve performance through optimization of the channels.

Keywords: Multi-stage flash desalination; Demister; Anti-re-entrainment; Experiment; Numerical simulation

1. Introduction

So far, some regions around the world still face freshwater shortage crises, and desalination of seawater is a feasible solution [1]. Multi-stage flash (MSF) evaporation technology are being broadly applied in fresh water production industry [2]. Currently, there are approximately 19,400 seawater desalination facilities in operation around the world, keeping the daily capacity of 99,700,000 m^3 [3]. There is an appreciable daily production of fresh water, but it consumes a large amount of electricity. Therefore, combining MSF with renewable energy to achieve a balance between input and output becomes an important development direction [4]. As one of the clean and renewable energy sources, solar energy has attracted widespread attention due to the characteristics of rich in resources and without exploitation. More noteworthy is that most water scarce areas often face large amount of solar radiation, which enables solar-desalination technology to be fully utilized. However, solar-desalination technology has also faced some challenges due to regional limitations and high facility investment [5]. Therefore, desalination technology

* Corresponding author.

with high energy efficiency is very important. Although newly developed techniques such as membrane separation is coming into use in some recently built facilities, they are meeting with the limitations of relatively lower treating capacity [6], which can well be addressed by thermal desalination approaches like MSF. Today, up to 40% of the global sea water desalination capacity is contributed by MSF [7], thanks to its advantaged in higher energy efficiency, lower infrastructure investment and high quality of distilled water [8]. Besides, MSF owns great potential in future application due to the combination of clean energy technology and environmental friendliness [9].

Any MSF process must satisfy the requirements of freshwater quality for the downstream industry applications or residential water demand, that is to maintain certain salinity level of distilled water. Therefore, it is a necessary operation in which saline water droplets being withdrew from the generated vapor flow, in this way, demister plays an important role in maintaining the quality of produced fresh water [10]. The most frequently used demisters in the field of thermal desalination are composed of wire mesh or wave-plates separators. Wire mesh has its strong ability to remove ultra-fine droplets under 15 μm, yet with the drawbacks of severe flooding and droplets re-entrainment [11–14]. Moreover, incrustation on the wire surface is hard to be avoided, leading to sharp increase in pressure loss and hence lower system energy efficiency [15,16]. By contrast, wave-plate demister owns the superiority of anti-flooding and much lower pressure loss. Although it is difficult for wave-plate demister to remove droplets smaller than 15 μm because of weak inertial, the problem can be tackled by installing drainage hooks into the passage for reorganizing the two-phase flow field [17].

However, in most conventional wave-plate demisters, droplets re-entrainment still occurs once the superficial flow velocity exceeds 3 m/s, under the effect of ultra-large shear stress between vapor flow and water film on the demister wall. Meanwhile, the additional drainage hooks can cause much larger pressure loss as compared to those without hooks [18], these phenomena strictly limit the improvement of treating capacity of entire MSF facility. In general, the performance of wave-plate demister is determined by plate geometry, droplets size and superficial flow velocity [19,20], among which droplets size and superficial velocity is pre-defined by operating conditions of desalination device, therefore, optimizing plate geometry should be of great essential to improve anti-re-entrainment performance of demisters to meet the needs for higher treating capacity.

Modern wave-plate demisters are basically comprised of blade and drainage channels, the profile of these geometries intensively influence the performance of the entire device. Commonly, there is balance to be achieved between the two performance indexes, that is, pressure drop and separation efficiency. For example, installing drainage channels can create stronger turbulence hence increase the probability of collision between droplets and wall, yet with the penalty of expanded pressure loss. Optimizing the geometry of wave-plate demister is the key to realize high removal efficiency with allowable pressure loss. It has to be mentioned that the ability of resisting droplets re-entrainment should be another important index, which has frequently been ignored in the design of demister. In other words, secondary droplets caused by re-entrainment must be taken into consideration.

Yu et al. [20] replaced conventional plates by those with streamline surfaces, the results indicated that pressure loss can be reduced significantly, yet with the penalty of lower droplets-removal efficiency. Tang et al. [21] numerically simulated the performance of sixteen different demisters with drainage channels, they proved that more turning bends or longer insertion length yields higher separation efficiency, but the sacrifice of larger pressure loss is also inevitable. For the purpose of achieving higher separation efficiency with moderate pressure loss, researchers coupled vortex generators (VGs) into the demister passage, it seems that better performance indexes can be obtained. For example, Liu et al. [22] installed tube bundle between adjacent plates at the inlet of the demister, the results indicated that separation efficiency can be improved to exceeds 95%, much higher than the tube-bundle-only or wave-plate-only structures, the authors attributed such phenomenon to the aggregation of droplets induced by the vortex array produced by the tube bundle. Yang et al. [23] conducted a comparative study on five different VGs installed in the passages, they found that rectangular VG owns the best enhancement performance, separation efficiency can be improved by 13.58% and the mean diameter at the exit decreased from 32.07 to 23.13 μm. The additional pressure loss brought by the above procedures is limited, however, coupling VGs into demister faces obstacles to scale application due to manufacturing difficulties.

In real MSF facilities, accumulated droplets trapped by demister will form liquid films on plate surfaces, which may lead to droplets re-entrainment into the mainstream. Re-entrainment occurs once the flow velocity exceeds some critical value where the surface tension inside film balances the shear force between vapor flow and liquid. The produced secondary droplets are the main reason for demister performance deterioration. However, re-entrainment was frequently ignored in previous simulation work, leading to underestimating separation efficiency [24]. For example, Liu et al. [22] and Yang et al. [23] in their experimental work reported droplets re-entrainment for various kinds of demister under high velocities, yet their simulations are conducted under lower operating conditions allowing for ignoring liquid film breakup. It is worth mentioning that droplets re-entrainment is especially remarkable in cases where VGs are used, because VGs accelerate local flow velocity and hence enhance shear force between mainstream flow and liquid film. It seems that, higher separation efficiency and moderate pressure loss is often received at the sacrifice of weaker anti-re-entrainment ability. Yuan et al. [25] carried out a computational work on the air-droplets flow and considered for the coalescence and breakup of droplets, the numerical prediction seems to be improved, yet interaction between droplets and liquid film is still not covered. Mao et al. [26] noticed that shear force causing film breakup is influenced by the plate's radius of curvature, so it can be inferred that trade-off also exists between pressure loss and anti-re-entrainment ability.

To the authors' knowledge, optimizing flow field in demister passage is the key to improve the overall

performance, particularly, large scale forced-vortexes must be reorganized to achieve such a goal. Researchers has conducted optimization work towards basic profile [20] of plate and drainage channel individually [21]. It must be pointed out that flow field is the result of combined effect of plate and drainage channel, hence optimization should be carried out on entire demister. In this study, a collaborative optimization is implemented by proposing a new-type demister equipped with innovative embedded drainage channels. The organization structure of this paper is as follows. In Section 2, the construction of the experimental platform and test section, as well as the settings and specific assumptions of the physical model are introduced. In the first part of Section 3, the comprehensive performance of the demister is evaluated through experiments and numerical simulations. The influence of plate spacing and inlet velocity on separation efficiency and pressure loss is studied. The remaining part of Section 3 models and calculates droplets aggregation and liquid film behavior in the simulation. In particular, through detailed flow field analysis, the impact of embedded drainage channel structures on anti-re-entrainment performance is revealed. Finally, the advantages of the proposed demister are demonstrated by comparing it with traditional structures in published literatures. The conclusions are drawn in Section 4 of the paper.

2. Experimental and numerical setup

2.1. Experiment

2.1.1. Test facility

The schematic diagram of the experimental facility is shown in Fig. 1, which is designed and constructed in the Jiangsu Key Laboratory of Green Process Equipment. The fluid is driven by a centrifugal fan with the power of 27.7 kW and maximum flowrate of 4,144 m^3/h. The open-loop wind tunnel owns the total length of 3,000 mm and the inner cross-section of 300 mm × 300 mm, the tunnel is produced from polymethyl-methacrylate material with high light transparency for the convenience of visualization. The bulk flow velocity can be continuously adjusted via a frequency converter (Type GD200A). The wind tunnel is operated in a suction mode to prevent possible leakage of liquid droplets. Atomization is realized through a compressed air circuit with stable supplying pressure of 0.4 Mpa and a liquid supplying pipe connected to a tank with supplying pressure of 0.3 Mpa. Air and water are mixed in six dual-fluid nozzles arranged in a 2 × 3 array placed at 800 mm to the upstream of the demister. A reversal liquid jet is adopted to ensure uniform droplets distribution at the entrance of the demister and isokinetic injection. Such atomization arrangement creates ultra-fine micrometer droplets smaller than 50 μm. Liquid is driven by a step-less speed regulated single-screw pump (0.125 kW, 35 m, 2.4 m^3/h), and the flowrate is measured by a glass-tube rotameter. A group of nine pressure taps are set 200 mm to up-and-downstream of the test section to obtain pressure loss across demister. Pressure data is acquired using digital micro-manometer (Type AS510). Flow velocity at the demister entrance is measured using an anemometer (Type AT816). Pressure and velocity are measured on several locations of the tunnel cross-section to obtain their arithmetic mean values. Catch basins are placed beneath each part of the wind tunnel to collect settled liquid and removed droplets by demister. When conducting experiments on demisters with different plate intervals, it is important to prevent droplets leakage from test section, hence the plates are kept in close contact with the walls on both sides of the tunnel. In addition, an environment of saturated humidity is sustained in the tunnel to prevent possible evaporation for the purpose of reducing measurement error. An electronic balance is equipped to measure the weight of collected liquid under the test section for calculation of separation efficiency. The range and accuracy of the instruments used in the experiment are summarized in Table 1.

2.1.2. Test section

Demister plates are 3D-printed using resin material and placed parallel to the axis of the wind tunnel. The thickness of the demister plates is 3 mm. Equal intervals

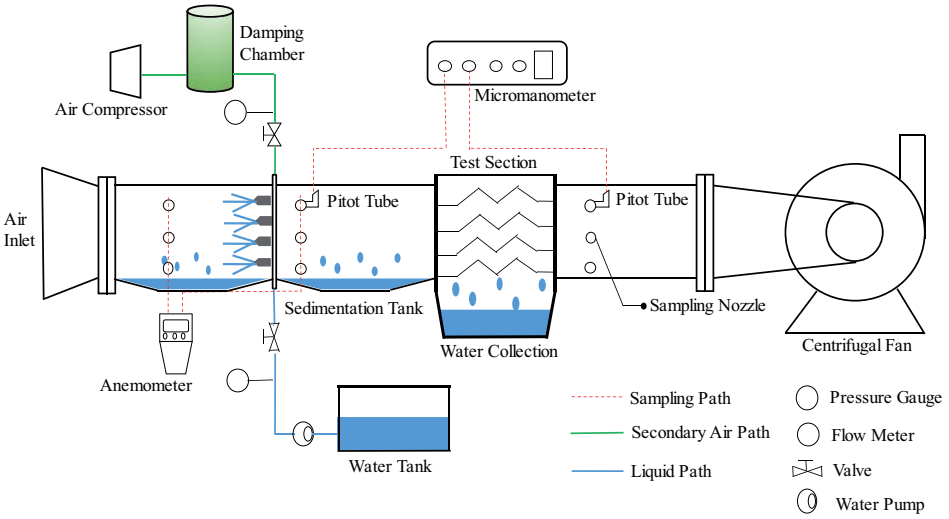

Fig. 1. Schematic diagram of the experimental system.

between adjacent plates are strictly controlled through a set of buckles, the intervals can be adjusted within the range of 22–30 mm. Axial positions of each plates are aligned via four steel rods installed at the corner of the demister. Surrounding wall of the test section is made from transparent polymethyl methacrylate with the thickness of 10 mm. A picture of the test section is shown in Fig. 2.

2.1.3. Measurement uncertainty of separation efficiency

Separation efficiency η is defined using Eq. (1).

$$\eta = \frac{M_c}{M_{in} - M_s} \times 100\% \tag{1}$$

where M_c is the weight of collected water, kg, M_{in} is the weight of supplied water, kg, and M_s is the weight of water in the sedimentation tank, kg.

Droplets filtered by demister are discharged into a water collection tank through an orifice plate. Array of the holes on the plate is carefully designed to realize rapid drainage, therefore, to ensure accurate measurement of M_c. Meanwhile, the accumulated liquid on the floor of the tunnel may be blown downstream causing so-called "pseudo-re-entrainment", therefore, height of the demister plates is made taller than that of the tunnel to strictly distinguish liquids being collected and re-entrained. Furthermore, directing baffles are added to the up-and-downstream of the demister to enhance liquid collection.

Separation efficiency in the experiment is measured indirectly, thus the uncertainty analysis is performed according to the method provided by Moffat [27]:

$$e = \sqrt{\sum_{i=1}^{n} \frac{\partial W}{\partial x_i} \Delta x_i^2} \tag{2}$$

Table 1
Range and accuracy of the instruments

Apparatus (model number)	Measuring range	Precision
Anemometer (HC-001)	0.1–30 m/s	±5%
Electronic scales (KF-30)	3,000 g	1 g
Pressure gauge	0–1.6 MPa	±2.5%
Rotor flow meter (LZB-15F)	25–250 L/h	±2.5%
Micromanometer (AS510)	0–0.01 Mpa	3 Pa

where e stands for the overall uncertainty of the target performance parameter; W is the estimation of the wanted parameter; x_i and Δx_i indicate the i-th independent variable and its associated error. Using Eq. (2), the measurement uncertainty of separation efficiency considering for droplets re-entrainment is estimated to be 3.8%, which is within a reasonable range.

2.2. Computational setup

2.2.1. Computational domain

Geometry of single plate assembling the demister is shown in Fig. 3, which is consistent with that used in the experiment. The profile of the plate surface is basically streamline for the purpose of reducing pressure loss. Two embedded drainage channels, namely, Embedded Channel_1 (EC_1) and Embedded Channel_2 (EC_2) are arranged along the longitudinal direction. The overall length of the plate is less than half of most conventional defogging plates, representing a space-saving design. It has to be mentioned that both drainage channels are integrated into the plate, therefore the apparent profile of the entire plate is kept streamlined even with hooks. EC_1 is surrounded by Hook_A and Hook_B, while Hook_C is located to the downstream of EC_2. Since the height of the plate is much longer than their intervals, the flow field can be assumed to be two-dimensional. The repeated flow pattern in each passage allows for the adoption of transverse periodic boundary condition. therefore, the computational domain is enclosed by inlet, outlet, plate wall and extended periodic boundaries, as illustrated by Fig. 4a. Noting that 2D calculation is adopted only providing convenience for parametric study of pressure loss and separation efficiency without re-entrainment. When accounting for liquid film behavior and re-entrainment, 3D calculation is employed and its computational domain and boundary conditions are presented in Fig. 4b. The values of the parameters defined in Fig. 4a and b are listed in Table 2.

2.2.2. Two-phase flow modeling

The two-phase flow in the demister channel is fully developed turbulence with the Reynolds number of over 4,700. Thus, the turbulence SST k–ω model is adopted to close the Navier–Stokes equations, which is proved to be quite applicable in the flow field computation of demisters [28]. The model equations are:

Fig. 2. A picture of the test section.

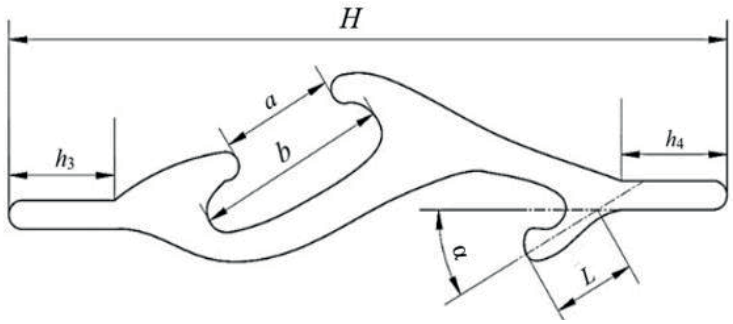

Fig. 3. Geometry and parameter definition of demister plate.

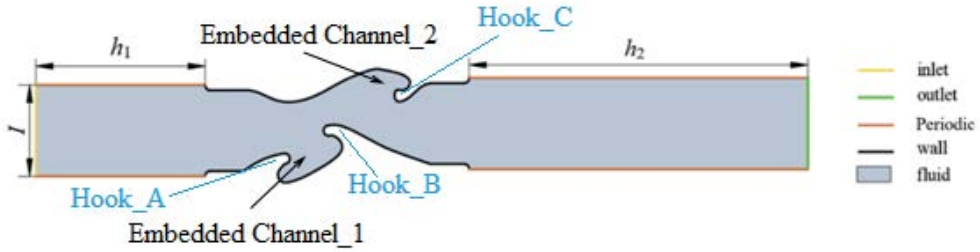

(a)

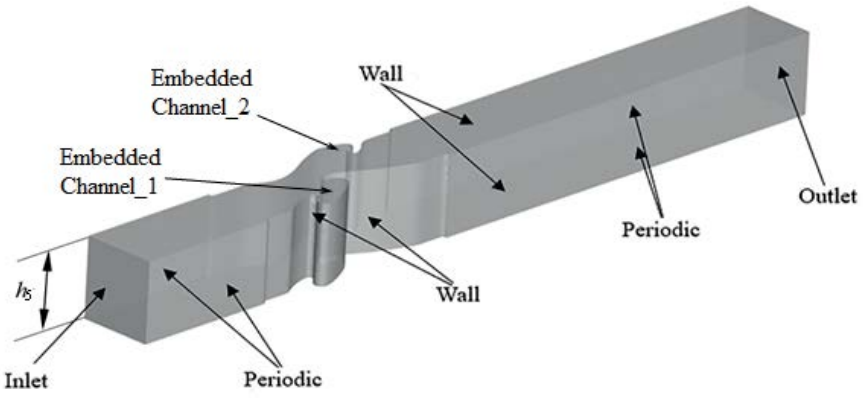

(b)

Fig. 4. Computational domain and boundary conditions: (a) two-dimensional and (b) three-dimensional.

$$\frac{\partial}{\partial x_i}\left(\rho k u_i\right)=\frac{\partial}{\partial x_j}\left(\Gamma_k\frac{\partial k}{\partial x_j}\right)+G_k-Y_k$$

$$\frac{\partial}{\partial x_i}\left(\rho\omega u_j\right)=\frac{\partial}{\partial x_j}\left(\Gamma_\omega\frac{\partial \omega}{\partial x_j}\right)+G_\omega-Y_\omega+D_\omega \tag{3}$$

where G_k and $G\omega$ stands for the production of turbulence kinetic energy k and dissipation rate ω, respectively. Γ_k and $\Gamma\omega$ are the effective diffusion coefficient. Y_k and $Y\omega$ represent the dissipation of k and ω due to turbulence, respectively. $D\omega$ is the cross-diffusion term.

Droplets motion is dominated mainly by the air drag force, hence the governing equation can be expressed as:

$$\frac{du_p}{dt}=F_D\left(u_g-u_p\right)+\frac{g\left(\rho_p-\rho_g\right)}{\rho_p}+F_X \tag{4}$$

where the first term on the right-hand of Eq. (4) stands for the drag force exerting on unit mass of droplets. F_D depends on the Reynolds number, droplets size, viscosity and droplets density, hence it is calculated by:

$$F_D=\frac{18\mu}{\rho_p d_p^2}\frac{C_D\mathrm{Re}_p}{24} \tag{5}$$

where d_p is the droplets diameter, Re_p is the droplets Reynolds number, which is defined by Eq. (6):

Table 2
Baseline values of the structural parameters

Parameter	Value
I	22, 24, 26, 28, and 30 mm
h_1	50 mm
h_2	100 mm
h_3	10 mm
h_4	10 mm
h_5	10 mm
H	78 mm
$D(a/b)$	0.6
L	8 mm
α	30°

$$\mathrm{Re}_p = \frac{\rho d_p \left| u_g - u_p \right|}{\mu_g} \tag{6}$$

The drag coefficient C_D in Eq. (5) is determined by Reynolds number, that is,

$$\begin{aligned} C_D &= \left(1 + \frac{1}{6}\mathrm{Re}^{2/3}\right) \cdot \frac{\mathrm{Re}}{24}, \ \mathrm{Re} \le 1000 \\ C_D &= 0.424, \ \mathrm{Re} > 1000 \end{aligned} \tag{7}$$

where F_X accounts for all additional forces exerting on droplets including pressure gradient force, virtual mass force and Saffman lift force.

The effect of turbulence dispersion on droplets motion is considered by using the random walk model, which incorporates the fluctuating velocity of the continuous phase into calculation.

Velocity slippery between droplets can lead to collision, then either coagulation or rebound may occur without considering for the breakup of any single droplet due to their small size. The random collision model is employed which utilizes the concept of collision volume to calculate the probability of droplets collision [29], the definition equation is:

$$K = \frac{\pi\left(r_1 + r_2\right)^2 U_{\mathrm{rel}} \Delta t}{V} \tag{8}$$

where r_1 and r_2 are the radius of the two droplets into collision, respectively. U_{rel} is the slip velocity of the two droplets considered. Δt is the time step, and V stands for the volume of the continuous phase unit where droplets r_2 locates. A critical value is b_{crit} used to decide whether coagulation or rebound takes place once two droplets come into collision, which is defined using the following equations:

$$\begin{aligned} b_{\mathrm{crit}} &= \left(r_1 + r_2\right)\sqrt{\min\left(1.0, 2.4 f / \mathrm{We}_c\right)} \\ f\left(r_1 / r_2\right) &= \left(r_1 / r_2\right)^3 - 2.4\left(r_1 / r_2\right)^2 + 2.7\left(r_1 / r_2\right) \\ \mathrm{We}_c &= \rho U_{\mathrm{rel}}^2 \bar{D} / \sigma \\ b &= \left(r_1 + r_2\right)\sqrt{Y} \end{aligned} \tag{9}$$

where We_c is the collision Weber number, D stands for the arithmetic mean diameter of the two droplets considered. ρ and σ are the density and surface tension of droplets, respectively. Y represents a random value between 0 to 1. Occasions of $b < b_{\mathrm{crit}}$ and $b > b_{\mathrm{crit}}$ denotes coagulation and rebound between droplets, respectively.

The Euler-Wall-Film model is employed to describe the behavior liquid film on the plate surface. The governing equations are:

Mass conservation equation:

$$\frac{\partial \rho_1 h}{\partial t} + \nabla_s \cdot \left(\rho_1 h \vec{V}_1\right) = \dot{m}_s \tag{10}$$

Momentum conservation equation:

$$\begin{aligned} \partial h\vec{u}_l / \partial t + \nabla_s \cdot \left(h\vec{u}_l\vec{u}_l\right) = -h\nabla_s P_L / \rho_l + \left(\vec{g}_\tau\right)h + 3\vec{\tau}_{\mathrm{fs}} / \left(2\rho_l\right) \\ - 3\mu_l \vec{u}_l / \left(\rho_l h\right) + \dot{q} / \rho_l \end{aligned} \tag{11}$$

where h and $\vec{u}_l$ are the thickness and mean velocity of liquid film, respectively. ρ_l is the liquid film density. ∇s denotes the surface gradient operator. $\dot{m}_s$ stands for the mass source from the interaction between film and wall on unit surface area. $\dot{m}_s$ and μ_l are the gravity component parallel to the direction of the liquid film and dynamic viscosity of the liquid film, respectively. $\vec{\tau}_{\mathrm{fs}}$ represents the shear stress on the interface of continuous phase and liquid film. q and P_L represent momentum source and local pressure of continuous phase, P_L covers the combined influence of vapor flow, diffusion and surface tension.

The behavior of droplets-film interaction depends on the impact energy, which is expressed as:

$$E^2 = \frac{\rho_p V_{p,n}^2 d_p}{\sigma}\left(\frac{1}{\min\left(h / d_{p,1}\right) + 1/\sqrt{\mathrm{Re}}}\right) \tag{12}$$

where $V_{p,n}$ denotes the normal velocity component of droplets with respect to the film surface being impacted. σ is the film surface tension. The Reynolds number Re in Eq. (13) is defined by:

$$\mathrm{Re} = \frac{\rho_p V_{p,n} d_p}{\mu} \tag{13}$$

Judgment of collision mode obeys the following rule:

$E < 16$, droplets adhere to the film keeping their spherical shape;

$16 \le E < 57.7$, droplets spread into films;

$E \ge 57.7$, splashing occurs and secondary droplets are produced.

When the shear action of the airflow on the liquid film is large, the liquid film breakup occurs. That is, when the shear stress exceeds the critical value, re-entrainment occurs. Through extensive simulations and comparison with experimental results, the measured critical inlet velocity is gradually approached, and the final critical shear stress is determined to be 20 Pa. That is, for the structure in this

work, when the shear stress exceeds 20 Pa, the liquid film breakup and re-entrainment occur.

The mass flow rate of the stripped film is calculated by:

$$\dot{m} = C\frac{9}{2}\rho_l \omega \lambda_{\min} \tag{14}$$

where C is mass coefficient which equals 0.5. ρ_l is liquid film density, the wave of length λ is formed on the liquid film due to Kelvin Helmholtz type instability, $\lambda_{\min}$ is calculated using Eq. (15). These waves are damped by the viscous effect in the membrane. Balance between wave growth and damping provides a term for the frequency ω, determined by Eq. (16).

$$\lambda_{\min} = 2\pi^3\sqrt{16}\left(\frac{\mu_l\sqrt{\sigma/\rho_l}}{\beta\rho_g V_g^2}\right)^{2/3} \tag{15}$$

$$\omega = 0.384\frac{\rho_g V_g^3}{\sigma}\sqrt{\frac{\rho_g}{\rho_l}} \tag{16}$$

where μ_l is dynamic viscosity of liquid film, σ is surface tension of the film. The sheltering parameter β equals 0.3. ρ_g and V_g droplet density and velocity, respectively. Initial velocity of secondary droplets from film breakup is determined by the velocity of the moving film, and the average size of secondary droplets is defined by:

$$\bar{d} = F_N \cdot \frac{9}{2}\lambda_{\min} \tag{17}$$

where F_N is the diameter coefficient, which equals 0.01.

In this study, following assumptions are proposed in the numerical simulation:

- The gas is considered incompressible because the Mach number is relatively low (far below 0.1).
- Considering for the isothermal environment and saturated conditions, heat transfer and evaporation are ignored.
- Neglecting the effect of edge separation on the liquid film in the Euler-Wall-Film (EWF) model [30].

2.2.3. Numerical solution and boundary conditions

The computation is conducted using the finite-volume-based solver FLUENT 2022. Second-order-upwind scheme is used for pressure discretization and first-order-upwind scheme is chosen for turbulent-related quantities. To ensure optimal convergence, velocity and pressure fields are directly coupled using "coupled" algorithm. The iterative residual is set to 1×10^{-5}, besides, droplets concentration at the outlet is monitored to help judging whether the computation is converged. The continuous phase is regarded incompressible and its viscosity follows the rule of Sutherland Law. Uniform velocity within the range of 1–9 m/s is imposed to the inlet and constant atmospheric pressure is set at the outlet. Droplets with the surface tension of 0.0727 N/m are adopted as the discrete phase. Uniform surface injection normal to the inlet boundary is employed in both 3D and 2D calculations. The initial velocity of droplets is set to be identical with the continuous phase. In 2D calculation, mass concentration of the droplets at the entrance is 5×10^{-9} kg/m^3. While during 3D calculation, the inlet droplets concentration is set to be 0.007 kg/m^3. Size of the droplets falls within the range of 5–50 μm, and their distribution obeys the Rosin–Rammler pattern with the mean diameter of 20 μm and the spread coefficient of 1.9. The boundary conditions for numerical simulation are in accordance with that in the experiment.

2.2.4. Grid scale sensitivity

The computational mesh is generated using mesh tool software ICEM CFD. Given the complexity of the computational domain, unstructured quadrilateral mesh system is adopted for 2D cases. Dense mesh is used near the wall for the purpose of capturing flow details. Thickness of the first layer next to the wall is 0.01 mm which guarantees a Y-plus level lower than 2. The growth rate is set to be 1.2, and the maximum cell unit in the core region of the ducts is 0.16 mm. Mesh in the extended parts to the up-and-downstream of the passage is sparse with the size of 0.4 mm. Identical mesh settings are used in 3D cases except for the hexahedron grids. The global computational mesh and details near hooks in 2D cases are shown in Fig. 5a. The 3D mesh is shown in Fig. 5b.

In order to balance accuracy and cost-effectiveness in calculation, grid independence analysis is conducted. Five different mesh systems are generated for 2D case with the plate interval of 22 mm, the cell numbers are 11,024; 31,682; 52,434; 112,883 and 163,283. Numerical simulations are then performed with inlet velocities of 3–9 m/s. The calculation results are shown in Fig. 6. Research has found that once the total number of cells exceeds 52,434, not only does the pressure loss become stable, but the solution of the discrete term also gradually stabilizes, hence consistent mesh strategy was adopted for all cases in the following computations.

3. Results and discussion

3.1. Overall performance

The influence of plate interval and inlet velocity upon separation efficiency is investigated through experiment, as illustrated by Fig. 7a. It can be seen that plate interval greatly affects the separation efficiency. Within the operating conditions lower than 4 m/s, increasing inlet velocity sees a remarkable improvement of separation efficiency for smaller intervals, yet for larger intervals the improvement becomes weak. As the interval increases from 22 to 30 mm, separation efficiency decreases by 27%, which could be explained by the fact that the reduced maximum velocity magnitude and weaker turbulence lead to lower inertia, which is the key mechanism governing droplets interception. For the plate interval of 22 mm, increasing velocity from 3.13 to 5.25 m/s sees an improvement of separation efficiency of up to 72.89%. For larger plate interval of 30 mm, increasing velocity from 3.5 to 8.5 m/s yields efficiency improvement of up to 59.5%, yet still much lower

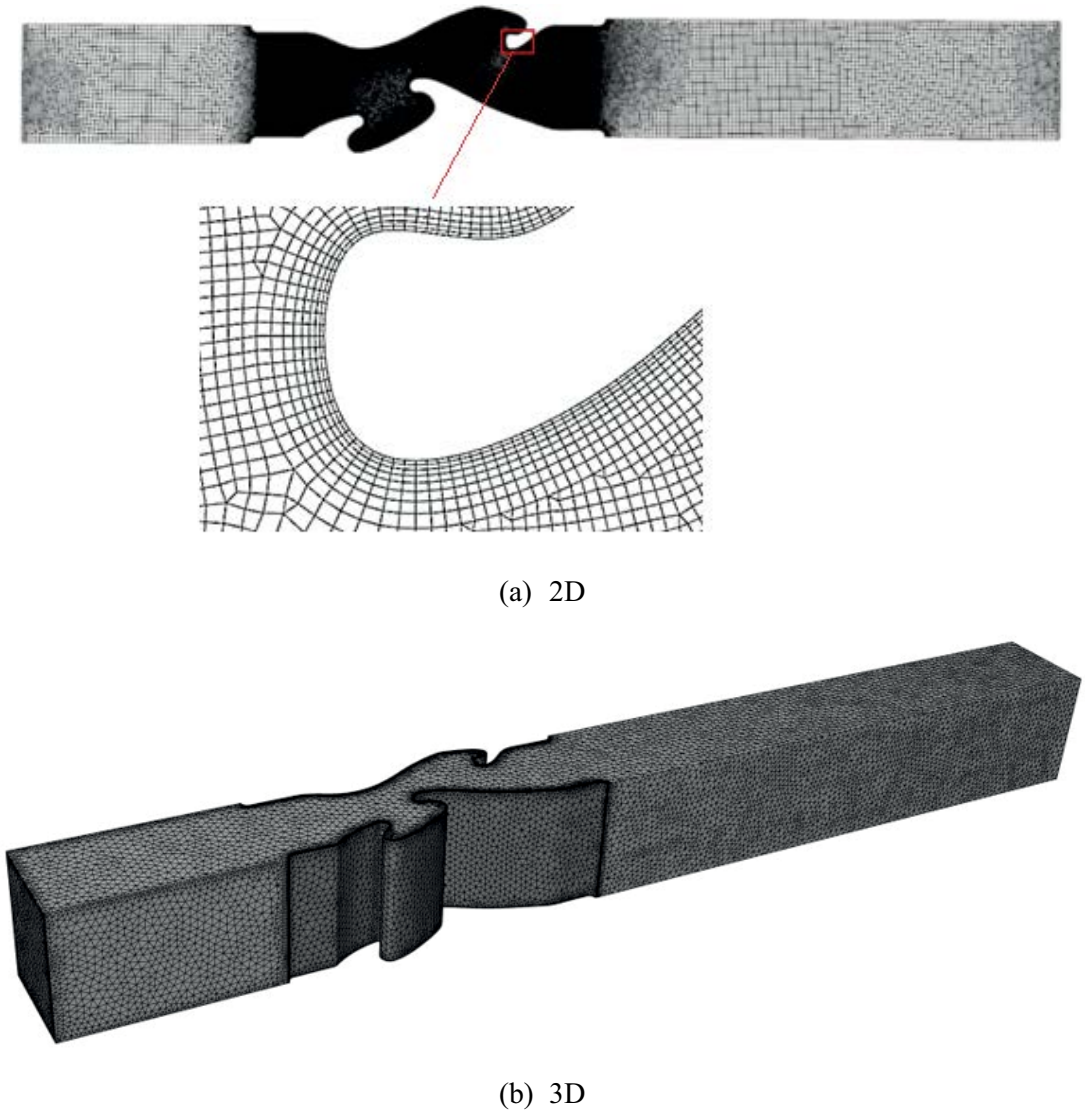

(a) 2D

(b) 3D

Fig. 5. Computational mesh.

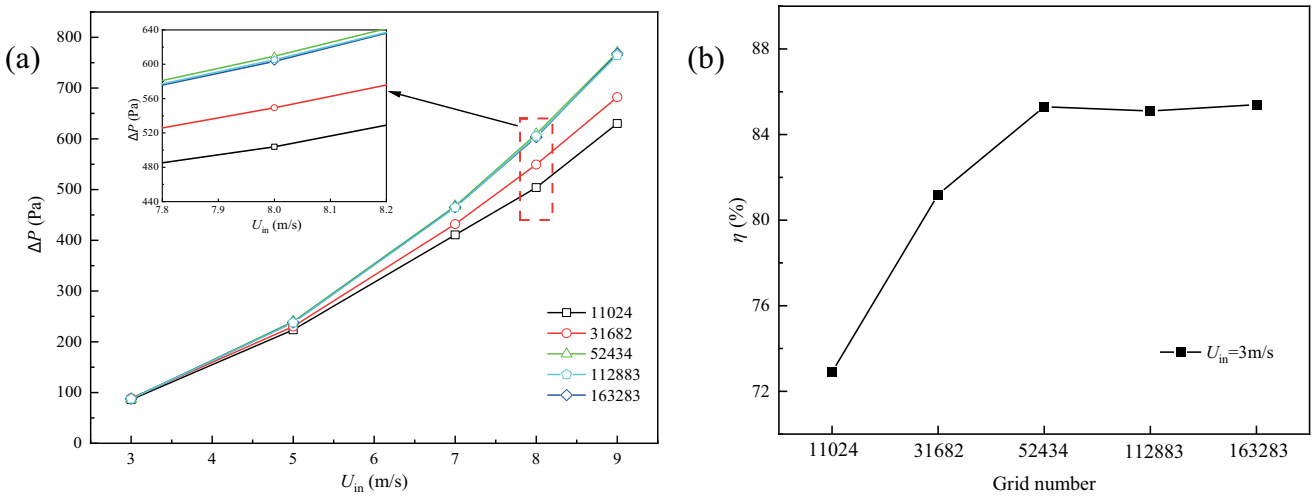

Fig. 6. Variation of pressure loss against inlet velocity: effect of mesh scales.

than the efficiency created by I = 22 mm at lower velocity of 3.13 m/s. The above-described phenomenon can be well described by non-dimensional Stokes number defined by Eq. (18). It is clear that higher velocity or smaller plate interval can create lager St number, which means that droplets are easier to be detached from the mainstream and thus removed. Noting that plate interval I is chosen to be the characteristic length in the definition of Stokes number.

$$\mathrm{St} = \frac{\rho_p U d_p^2}{18\mu I} \tag{18}$$

It can be known from Fig. 7a that, the improving trend of separation efficiency against inlet velocity slows down and it reverses upon some critical point after which the efficiency decreases if further increasing flow velocity. This observation can be attributed to the following reasons: (1) Larger droplets are almost completely captured by the demister at higher velocities, while smaller droplets are still difficult to be trapped due to limited inertia, that is, separation efficiency meets its bottleneck if solely relying on increasing velocity; (2) Liquid films are detached from the plate surface under the effect of strengthened shear force produced by higher flow velocity near the wall, producing so called re-entrainment. Before reaching critical velocity, re-entrainment can be offset by increased interception of droplets thanks to greater inertia. However, once velocity exceeds its critical point, breakup of liquid film gets drastic. Moreover, splashing occurs due to stronger impact between droplets and liquid film, producing secondary droplets which are much smaller in size, leading to efficiency deterioration. The experimental result shows that, for the narrowest plate interval of I = 22 mm, the critical velocity appears to be 5.25 m/s, while it increases to 8.5 m/s when plate interval expanded to 30 mm. Thus, it can be inferred that re-entrainment can be delayed simply by increasing plate interval, however, the drawback is that separation efficiency becomes lower especially at lower velocities.

A general understanding is that higher critical velocity means stronger anti-re-entrainment ability; however, this is achieved at the sacrifice of overall lower separation efficiency. To be specific, the critical velocity of I = 24 mm is relatively lower, nevertheless, its separation efficiency in the re-entrainment conditions is still higher than those with larger plate intervals without re-entrainment taking place. Hence it can be deduced that anti-re-entrainment performance of demister is influenced by not only inlet velocity, but also internal flow field details.

Although separation efficiency can be well improved by adopting narrower plate intervals, pressure loss also increases with more compact plates group, as indicated by Fig. 7b, that pressure loss increases remarkably with reducing plate interval, the difference is more notable at higher inlet velocities. It is also noticed that the dropping trend of pressure loss has its limitation with expanding plate interval, which is expected to be due to the specific flow field in the passage. It is a permanent goal to realize higher efficiency with lower pressure loss, that is, to achieve balance between droplets removal and system consumption. A new performance factor F is defined by Eq. (19) to complete a comprehensive evaluation:

$$F = \frac{\eta}{\mathrm{Eu}};\ \mathrm{Eu} = \frac{\Delta P}{\rho U_{\mathrm{in}}^2} \tag{19}$$

where Eu is the dimensionless Euler number characterizing pressure loss and η denotes the separation efficiency, the results are summarized by Fig. 8. It can be seen that performance factor F generally increases with expanding plate interval, thanks to the reduced pressure loss. It is worth noting that the advantage of larger plate interval is more prominent at higher velocities (≥7 m/s), which can be explained by the fact that sparse and compact plate arrangements produce comparable separation efficiencies as a result of distinct anti-re-entrainment abilities. Performance factors of smaller intervals (I = 22–24 mm) are relatively stable, while those of larger intervals (I = 26–30 mm) sees fluctuations

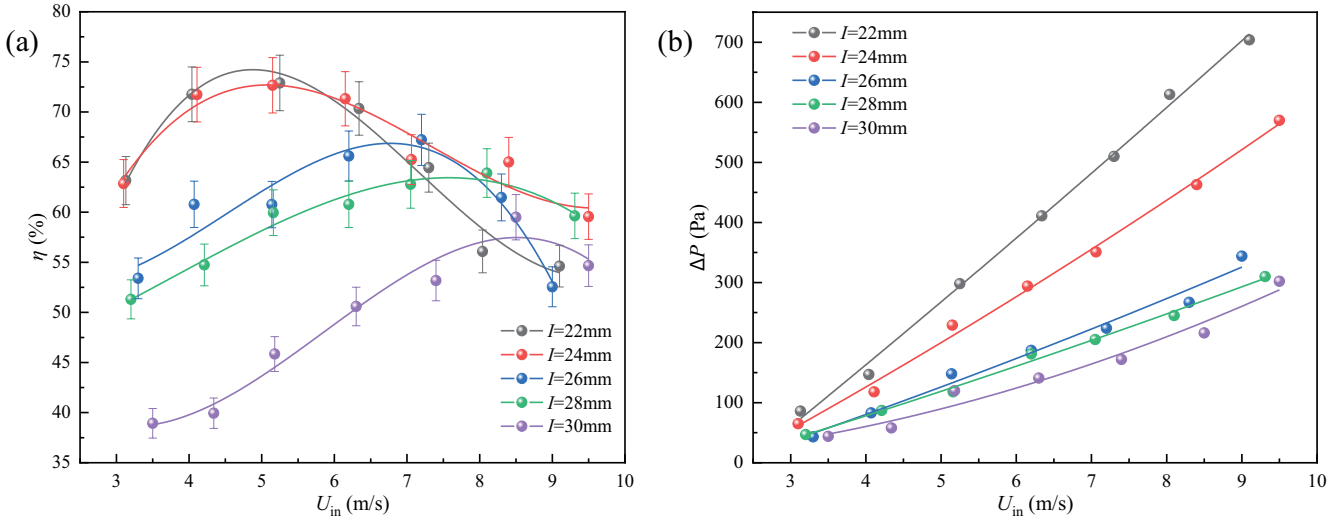

Fig. 7. Influence of inlet velocity and plate interval upon (experiment): (a) separation efficiency and (b) pressure loss.

which meet their highest level at higher velocities within the range of 7–9 m/s, indicating superior anti-re-entrainment and pneumatic performance of the new demisters.

3.2. Numerical validation

Computational results are compared with experimental data to assess the applicability of numerical model. Two different wall-boundaries for droplets are checked, namely, "Trap" denotes the wall treatment where droplets are collected once they collide with the plate surface, and EWF stands for the Euler-Wall-Film model. In this part, demister with the smallest plate interval of 22 mm is adopted for model validation in terms of pressure loss, considering for the higher turbulence level and hence largest mechanical loss through demister passage. Fig. 9a indicates that the adopted turbulence model agrees well with the measured pressure loss data, and that pressure loss solution is almost independent of droplets wall-boundary model. However, the "Trap" scheme failed to predict separation efficiency with sufficient accuracy especially beyond the critical velocity where droplets re-entrainment occurs, as presented by Fig. 9b. By contrast, the dropping trend of separation efficiency at higher velocities are successfully reproduced by the "EWF" scheme. Model validation of separation efficiency is carried out using the median plate interval of 26 mm, which is representative and thereby adopted for detailed analysis on the two-phase flow in the following sections. It is worth noting that the predicted critical velocity is also in good agreement with that observed in the experiment, indicating a good usability of the model in calculating separation efficiency within wide range. Quantitatively, the calculated separation efficiencies are constantly higher than their measured counterparts. Which can be explained by the fact that, the atomization system produces large amount of tiny droplets much smaller than the lower limit (5 μm) in the numerical setting, causing unavoidable escaping from the demister due to small inertia. Nevertheless, the average gap between measured and calculated separation efficiency falls within the range of 2%–12.5%, proving an overall acceptable performance of the computational method employing "EWF" scheme and the defined criterion for calculating re-entrainment.

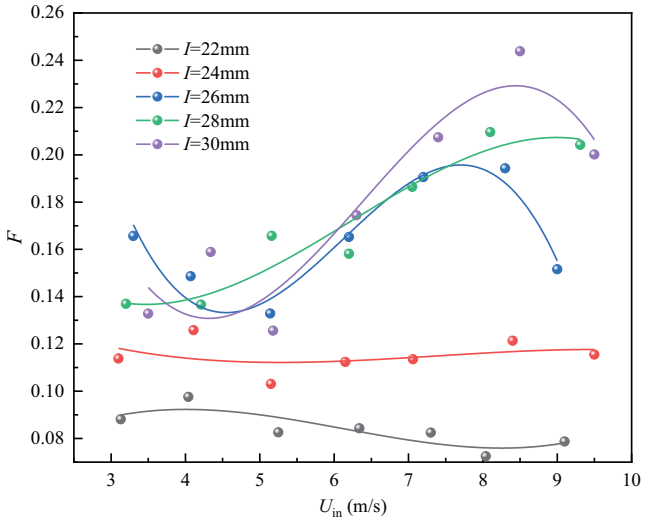

Fig. 8. Comprehensive performance of different plate intervals considering both separation efficiency and pressure loss (experiment).

To prove the understanding that larger droplets are nearly captured at higher velocities, simulations are conducted using "Trap" wall-boundary to obtain graded droplets separation efficiency. It can be known from Fig. 10 that separation efficiency consistently rises with increasing droplets diameter. For example, in the I = 22 mm case, separation efficiency improves from 18.48% at the velocity of 1 m/s to 98.42% at the velocity of 5 m/s for the D_p = 9 μm droplets group, as illustrated by Fig. 10a. By comparison, smaller droplets are quite hard to be trapped even accelerating velocity to a high level. Separation efficiency of the D_p = 1 μm droplets group is limited under 25% although velocity rises

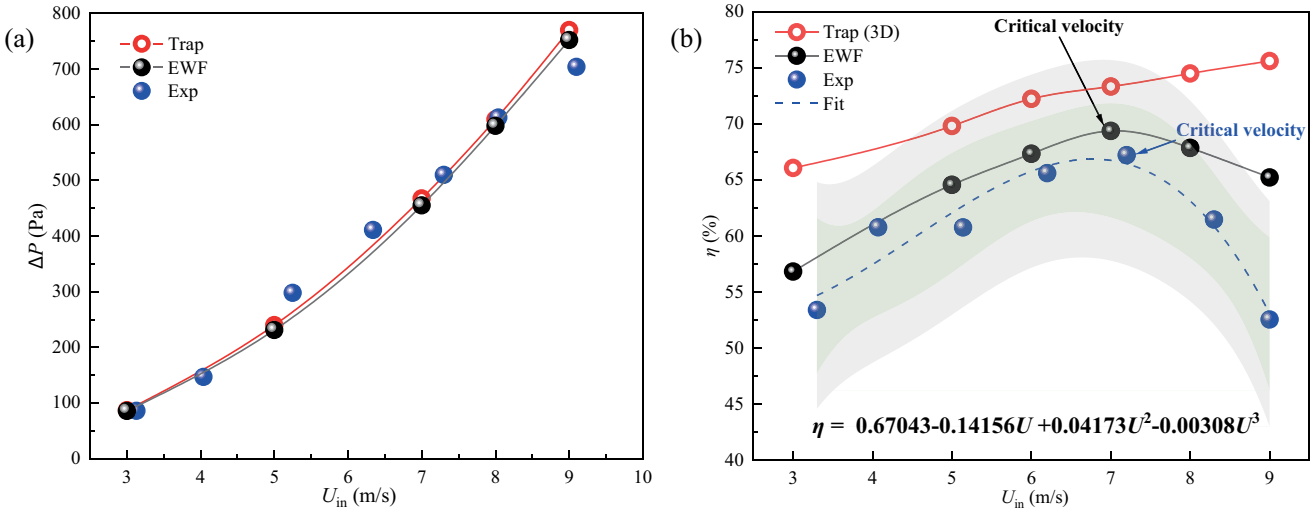

Fig. 9. Comparison between experimental and computational results: (a) pressure loss (I = 22 mm) and (b) separation efficiency (I = 26 mm).

up to 9 m/s. Noting that increasing velocity from 7 to 9 m/s sees a drop in efficiency for the D_p = 1 μm droplets group, which is attributed to strengthened turbulence carrying small droplets downstream. Fig. 10b shows that separation efficiency improves with decreasing plates interval, since narrower passages can create more curved streamlines, leading to stronger inertial effect for droplets to be detached from mainstream and collide on plate surface.

3.3. Flow field

It worth noting that, the apparent performances such as pressure drop, separation efficiency and anti-re-entrainment ability are closely related to the two-phase flow details in demister passage, therefore, it is a necessity to carryout flow field analysis to reveal such relationship, which is also helpful in particular optimization of plate geometry. To understand droplets behavior, their trajectories characterized by velocity magnitude are depicted in Fig. 11a–f, different plate intervals, inlet velocities and droplets diameters are compared. It can be see that larger droplets significantly reduce in the downstream because they are easier to be captured by the wall. Droplets are deflected near EC_1 and then intercepted by Hook_C. This deflection is more obvious for larger droplets than for smaller ones due to greater inertia. Comparing Fig. 11a and c, or Fig. 11b and d indicating that narrower plate interval promotes droplets interception not only by means of rising blocking ratio but also through flow field reorganization. To be specific, the increased maximum velocity upon Hook_B leads to more intensified centrifugal movement of droplets, making them easier to be intercepted by Hook_C. The influence of inlet velocity upon droplets motion obeys the same principle that higher velocity produces stronger inertia and hence more droplets collection, by comparing Fig. 11c and e, or Fig. 11d and f. Such comparisons also confirm the understanding that increasing size of droplets is more efficient than accelerating inlet flow for the purpose of improving separation efficiency, just as the definition of Stokes number which is proportional to velocity or to square of droplets diameter.

It must be pointed out that separation, pressure loss and anti-re-entrainment performance of demister is closely connected to the flow field in the passage, especially near the drainage channels. Fig. 12 presents the distributions of velocity and streamlines of different plate intervals under the inlet velocity of 5 m/s. It is evident that fundamental flow field is basically independent of the inlet velocity, except for the local flow acceleration with reducing plate interval. Embedded drainage channels realize a high level of surface integration making flow passage more smoothly, and hence help reduce pressure loss caused by hooks. The maximum local velocity in core region is several times larger than that of the inlet, which is frequently encountered in many kinds of demisters with tortuous passages. Interaction between near-wall weak flow and core flow accounts for large amount of loss, resulting in extra pressure drop. Fortunately, embedded drainage channels reduce the contact between these two flow motions and hence save the flow energy. Although pressure loss saving, separation efficiency is not much sacrificed because of the large-scale vortexes formed in the embedded drainage channels which entrained the droplets from turning back into the main stream. The vortex structures within the drainage channels are stable and unaffected by varying plate interval, pushing large droplets into the wall and entraining smaller ones until they are coalesced and eventually captured. The strong and stable vortexes in the embedded drainage channels also promote liquid film spreading and restrict growth of film thickness, hence droplets re-entrainment can be avoided.

Total pressure distributions of different plate intervals are presented in Fig. 13. For consistency, the pressure level is made non-dimensional, which is defined using the Eq. (20):

$$P_p = \frac{P_{in} - P}{\Delta P} \tag{20}$$

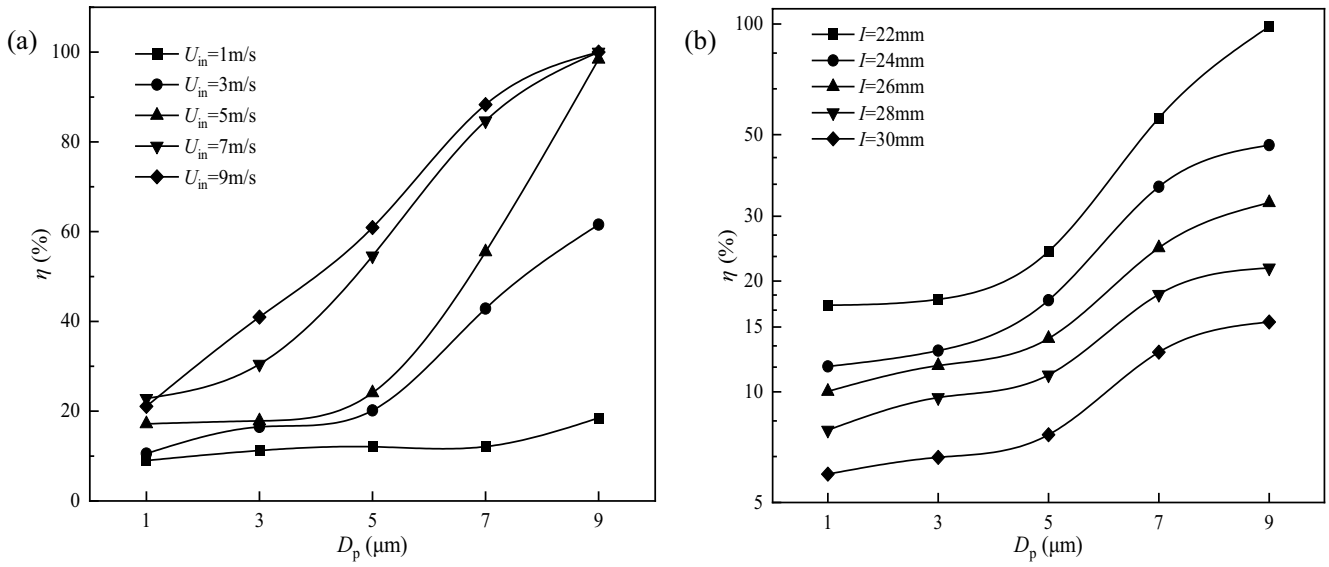

Fig. 10. Graded separation efficiency of demisters (computation): (a) effect of inlet velocity (I = 22 mm) and (b) effect of plate interval (U_{in} = 5 m/s).

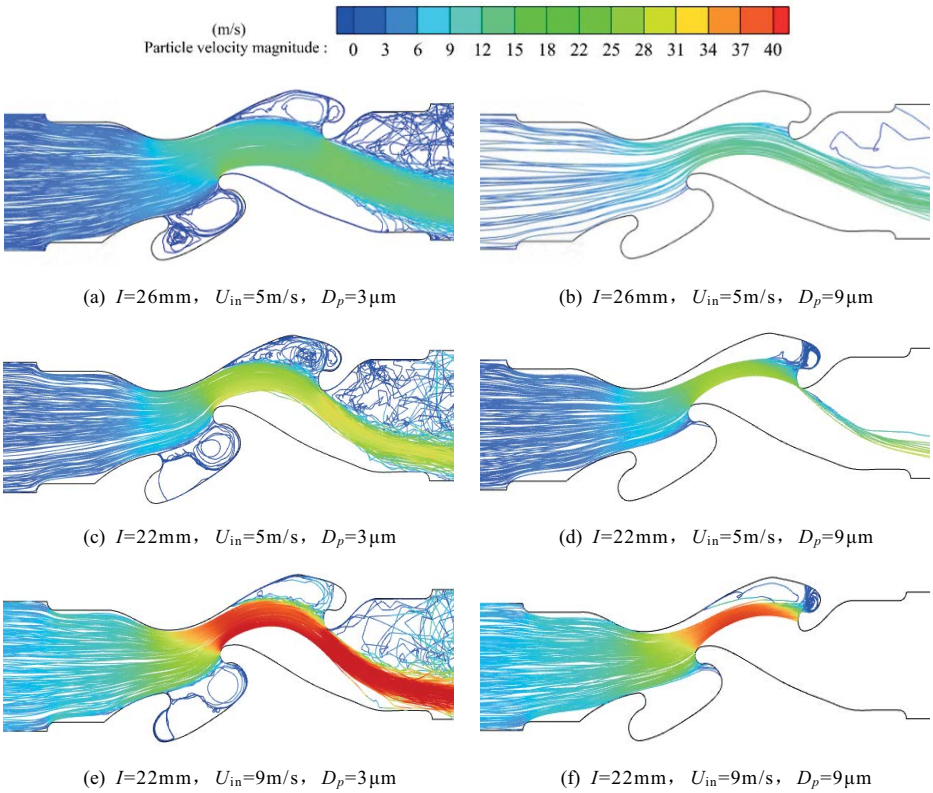

Fig. 11. Droplets trajectories in the plate channels: The influence of plate intervals, velocities and droplets diameters.

where P_{in} is the total pressure at the inlet; P denotes the local total pressure; ΔP stands for the pressure loss from inlet to outlet of the passage. It is noticed that pressure gradient from the core region to the leeward side of Hook_B is quite large, which means that flow separation in this area is the main source of pressure loss. By contrast, pressure gaps between core region and both embedded drainage channels are smaller, which implies that drainage channels produce minor pressure loss. Therefore, embedded drainage channel owns the advantage of superior separation performance achieved with minimum flow energy consumption.

The experimental result signifies that the optimum separation efficiencies are acquired at the inlet velocities of 5.3, 7.2 and 8.5 m/s for demisters with the plate intervals of 2, 26 and 28 mm, respectively, indicating re-entrainment comes into being at such operating conditions. Therefore, inlet conditions of 5–9 m/s in simulations are chosen to implement a detailed analysis. Since maximum local velocity is found at the tip of Hook_B, which is expected to be the main reason of liquid film breakup and hence droplets re-entrainment, detailed local velocity distributions are plotted along the tip wall-normal direction to examine the effect of near-wall velocity gradients, as presented by Fig. 14. Although transvers distribution of velocity appears to be quite uniform in the passage core, extreme high velocity peak (Within the range of 24.03 to 28.06 m/s) is found to be quite close to the tip wall just next to the viscous sublayer of merely 0.2 mm in thickness. Thus, re-entrainment is most likely to occur once liquid film thickness grows to over 0.2 mm, in other words, re-entrainment is prone to take place at the tip wall of the Hook_B.

3.4. Embedded drainage channel

By using the validated numerical approach, 3D simulations are implemented to check the liquid film distributions on the plate surface, as illustrated by Fig. 15, which is the mid-height cross-section. It can be found that liquid films are generally concentrated on the lateral sides of hooks just next to the tips where radius of curvature is small, which agrees with the aforementioned analysis on flow field presented by Figs. 12 and 13. These are exactly locations where shear forces are significant so that film breakup tends to happen, as noticed that film thickness near the tip of Hook_B rises from 0.242 to 0.593 mm with the inlet velocity accelerating from 3 to 7 m/s. However, further increasing inlet velocity to 9 m/s sees film reduction from 0.593 to 0.256 mm, which is the result of breakup. On the upper side of the plate shown in Fig. 15, liquid film grows on the windward of Hook_A and gradually spreads to inner side of the hook with increasing velocity. Meanwhile, liquid film concentrates on the distal end inside the EC_1 and rapidly spreads in the reverse direction on the wide surface of EC_1 instead of accumulating in the wall-normal direction. Therefore, liquid collection and anti-re-entrainment ability is enhanced on the upper side of the plate. The lower side of the plate shown in Fig. 15 also contributes to liquid collection thanks to its smooth surface profile which promotes liquid spreading

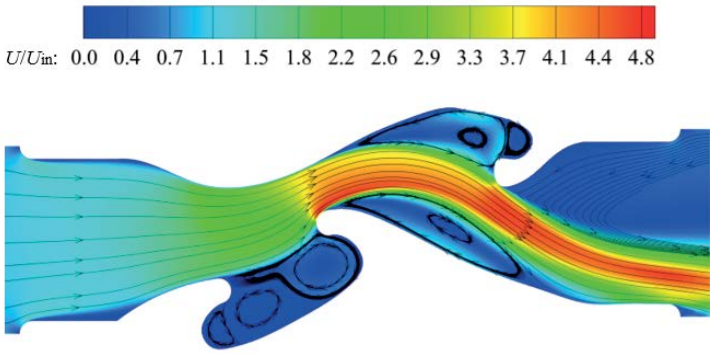

(a) *I*=22mm

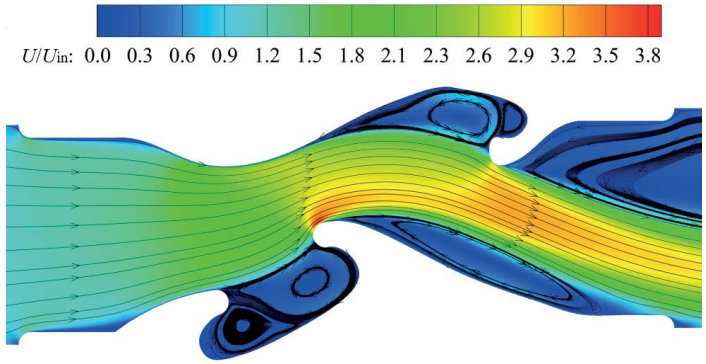

(b) *I*=26mm

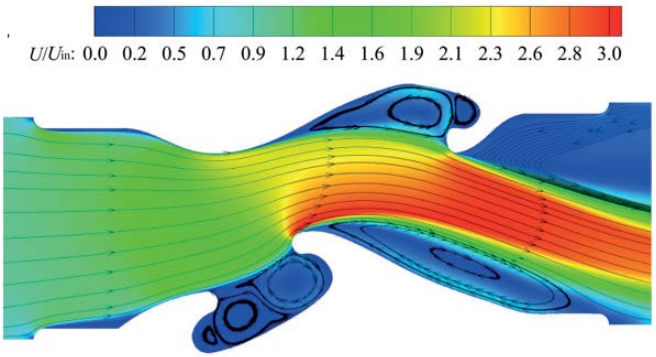

(c) *I*=30mm

Fig. 12. Contours of velocity magnitude in the demister passage (U_{in} = 5 m/s).

and prevents sharp increase of shear force and flow separation. It is also found that EC_2 induces the spread film to entry the inner side of Hook_C, which further enhances the liquid removal capability. The above analysis points out that the embedded drainage channels can suppress the occurrence of re-entrainment via re-organizing appearance of liquid film. In spite of that, film breakup is still inevitable on locations where large shear force dominates, specifically, it is limited on the small tip area of Hook_B and C.

Distribution of shear stress on plate surface under high velocity (U_{in} = 9 m/s) is presented by Fig. 16. Largest shear stress is produced on tip of Hook_B and C facing the flow, where film breakup is most likely to occur. While the rest of the plate surface is dominated by very small shear stress. In Fig. 17a linear variation of maximum shear against inlet velocity is presented. Noting that on any part of plate, once shear stress surpasses surface tension, film detachment takes place and secondary droplets be produced. Fig. 18 tells that film detachment starts to occur upon inlet velocity of 7 m/s and the mass of stripped liquid increases with flow acceleration due to the same reason. Beyond critical point, the amount of intercepted droplets is smaller than that of stripped film, and the gap widens with increasing velocity, leading to overall decreased separation efficiency. Also noticed is that liquid stripping is more remarkable on the upper side of the plate than on the lower side, which can be explained by the fact that EC_1 on the upper side withstands the strongest flow impingement and separation,

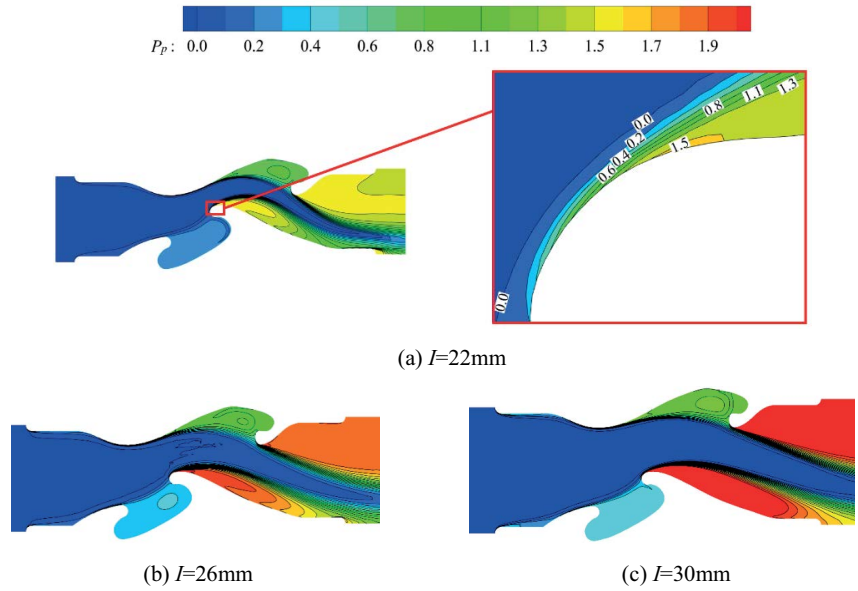

(a) I=22mm

(b) I=26mm (c) I=30mm

Fig. 13. Total pressure distribution in demister passage (U_{in} = 5 m/s).

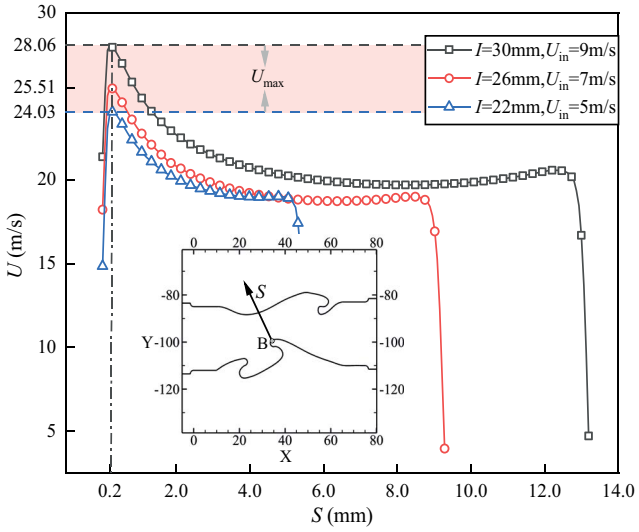

Fig. 14. Wall-normal velocity distributions at the tip of hook under various critical cases.

while EC_2 on the lower side faces relative weak flow. Therefore, reorganization of flow field by embedded drainage channels greatly affect liquid behavior in the demister passage.

It is known to all that droplets separation in tortuous passage is dominated by inertia principle, hence larger droplets are easier to detach from streamlines of continuous phase, impact on plate surface and be removed. For dense two-phase flow in the MSF devices, droplets aggregation is one important phenomenon that has often been ignored. Aggregation is generated basically by velocity slip between droplets, the outcome is positive because fine droplets coalesce into larger ones along passage which promote liquid collection. Fig. 19 presents the droplets trajectory characterized by velocity magnitude under the inlet velocity of 9 m/s, visible velocity slip is observed near both embedded drainage channels, which implies that aggregation occurs and helps promote droplets separation. EC_1 acts more effectively in promoting separation than EC_2, in terms of either creating velocity slip or preventing trapped droplets from re-entering the main flow, as illustrated by Fig. 20 that the upper surface of plate retains more liquid than the lower surface within entire range of inlet velocity. This can be attributed to the difference between profiles of the two sides, especially to the surrounding design of EC_1.

The aforementioned analysis implies that large scale swirling flow induced by embedded drainage channel plays an important role in droplets motion and liquid collection. Using the Ω criterion [31] defined by Eq. (21) to identify intensity of vortex inside EC_1.

$$\nabla V = \frac{1}{2}\left(\nabla V + \nabla V^{\mathrm{T}}\right) + \frac{1}{2}\left(\nabla V - \nabla V^{\mathrm{T}}\right) = A + B$$
$$\Omega = \frac{\|B\|_F^2}{\|A\|_F^2 + \|B\|_F^2 + \varepsilon} \tag{21}$$

where A and B are the symmetric and anti-symmetric tensions of the vortexes, respectively, ε = 0.001. As shown in Fig. 21, a pair of large scale counter-rotating vortexes are created inside EC_1 corresponding to two sites of high vorticity regions in the corners of the channel. These vortexes strengthen the immigration of droplets from mainstream into EC_1, trap them within the channel, and most importantly, spread the liquid film on the wide surface of EC_1. Therefore, better anti-re-entrainment performance can be realized on this side of the plate.

In the experiment, small amount of re-entrainment is unavoidably observed when flow velocity is high, as can be seen from Fig. 22 which records the secondary droplets attachment on the tunnel wall to the downstream of demister. The pictures are acquired under the inlet velocity of 8.5 m/s

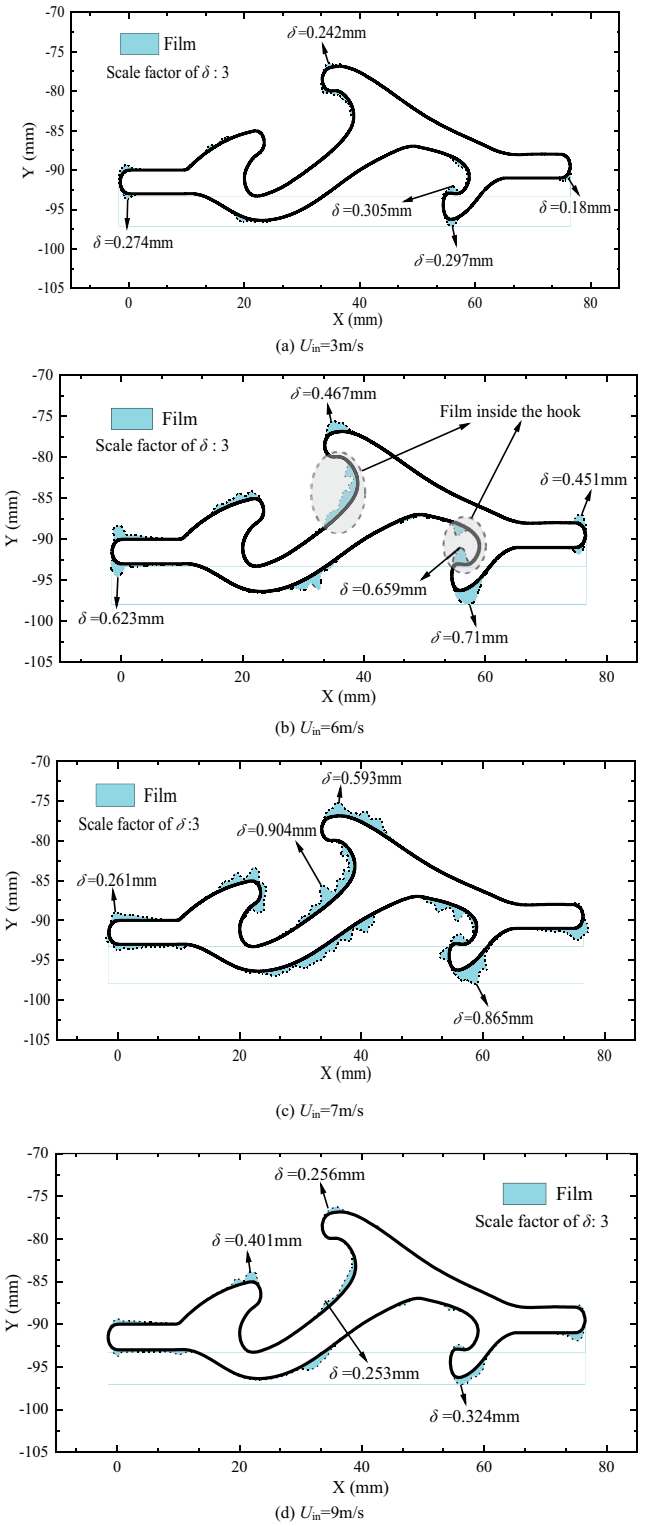

Fig. 15. Liquid film distributions on plate surface.

which is quite high to create re-entrainment in the passage. It can be noticed that liquid pile up at certain locations over time due to specific flow field produced by demister passage. The rapid accumulation of liquid at such point can be explained by the larger size of secondary droplets than the primarily sprayed fog droplets. The observed liquid mass behind demister mostly gathered in the lower part of the tunnel as a result of gravity that cannot be ignored for liquid film and ultra large secondary droplets. This effect is demonstrated by 3D simulation on two-phase flow, which shows that liquid film thickness increases along plumb direction, Fig. 23a. In fact, droplets re-entrainment and liquid drainage happen simultaneously, hence secondary droplets are more likely to be generated in the lower parts due to increased film thickness. Actually, secondary droplets are produced via various mechanisms depending on flow field as well as plate surface profile. As illustrated by Fig. 23b that rebound and splash dominate the first throttle region, and that film stripping mainly occurs at hook tip facing the flow where strong shear and separation dominate.

The advantage of the new demister with embedded drainage channels are proved via comparisons with conventional demisters studied by previous published papers, as presented by Fig. 24a. It has to be mentioned that in the experimental work of present study, atomization conditions are controlled carefully to produce quite fine droplets orders of magnitudes smaller than those used in former studies listed, therefore the overall separation efficiency of the I = 30 mm case appears to be lower due to much weaker inertia. Nevertheless, the proposed demister is superior to the conventional types in terms of its excellent anti-re-entrainment performance, that is, the critical velocity is increased significantly with embedded drainage channels. Some researchers [23,32] suggested installing VGs in the passage, which improve the probability of droplets collision on the wall, yet VGs themselves exacerbate re-entrainment, restricting the capability of demister. Other solutions like tube-bank [22] or porous foam [11] increases droplets interception yet with the penalty of much larger pressure loss, moreover, such component aggravate liquid coalescence on the wall which is easier to be stripped than to be discharged. Targeting on the identical droplets size with that in the literature receives higher separation efficiency with the present I = 22 mm case, yet with the penalty of reduced critical velocity, thus overall separation efficiency has to be balanced with anti-re-entrainment ability. Anyway, the proposed demister scheme provides higher comprehensive performance with great potential that further improvement is foreseeable through parametric optimization on the profile of embedded drainage channel. Comparing the comprehensive performance requires the same initial conditions to be set, like the consistency of droplet size distribution at the inlet, in order to be meaningful. The initial conditions in different literature are inconsistent, thus lacking comparability. However, it is worth noting that the literature provides separation efficiency and pressure loss for individual droplet sizes. Therefore, the comprehensive performance of 9 μm droplet studied in this article is compared with the comprehensive performance of 10 μm droplet in traditional demisters, as shown in Fig. 24b. it can be found that, the overall performance of the proposed demister with embedded drainage channels are superior to most recent enhancement designs, at least for 10 μm-Class droplets and even if pressure loss is considered.

Critical velocity with tube-bank and porous foam are 6 and 4.5 m/s, respectively, with VGs it reduced to 3.7 m/s,

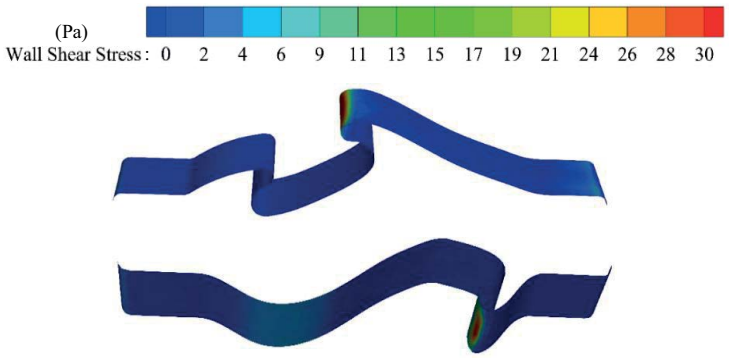

Fig. 16. Shear stress distribution (I = 26 mm, U_{in} = 9 m/s).

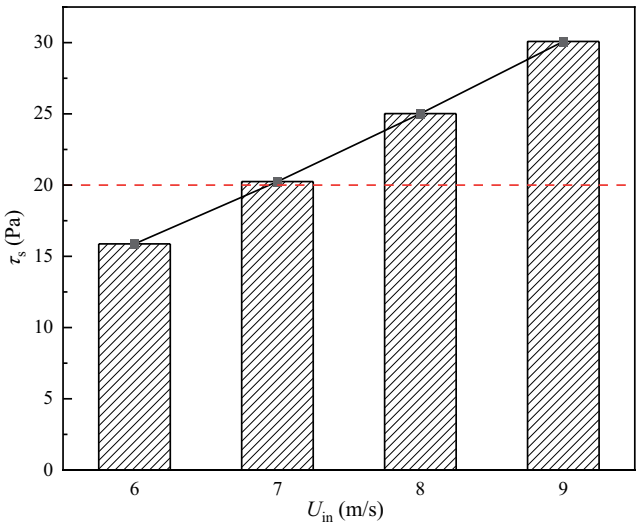

Fig. 17. Variation of maximum shear stress with inlet velocity.

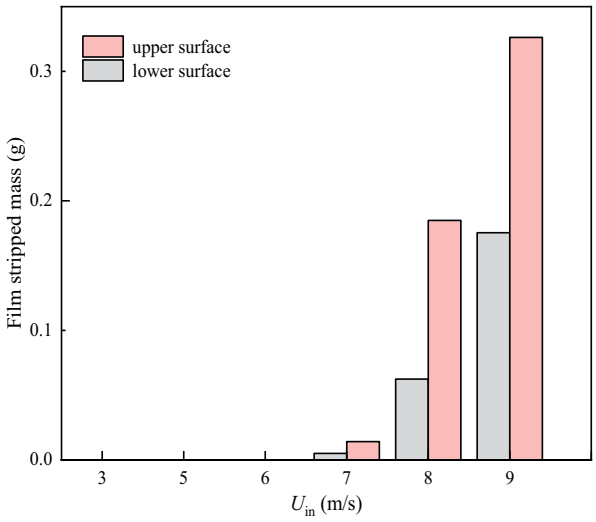

Fig. 18. Stripped mass of liquid with inlet velocity.

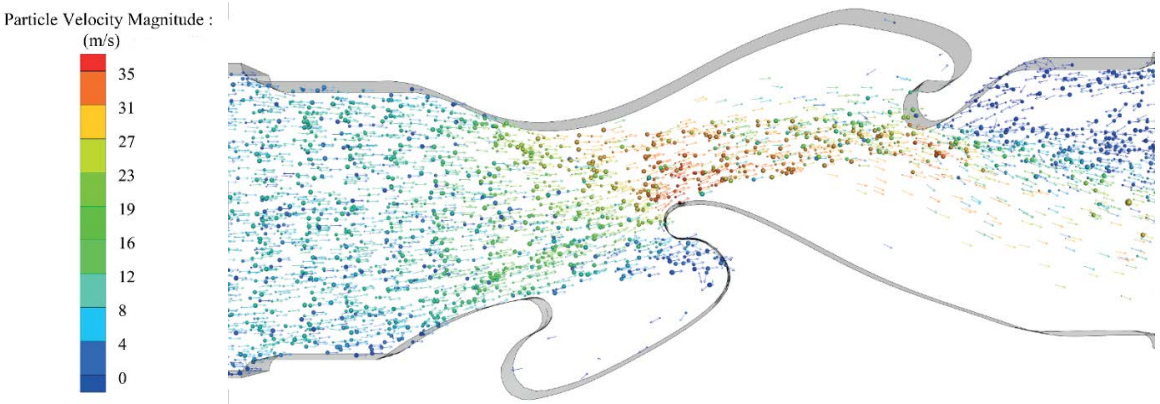

Fig. 19. Droplet tracking (U_{in} = 9 m/s, I = 26 mm).

indicating lower treating capability. Equipping embedded drainage channel improves the critical velocity to as high as 8.5 m/s in the I = 30 mm case of present study, implying strong anti-re-entrainment performance. Fig. 24c also gives the maximum flow velocity inside the demisters at critical point, which also signifies the ability in resisting re-entrainment. It can be seen that tube-bank and porous foam can only withstand internal velocity no higher than 17 m/s, with VGs the maximum internal velocity is reduced to be lower than 12.5 m/s. By comparison, embedded drainage channel can hold the maximum velocity of nearly 27 m/s even in the I = 22 mm case with relative lower critical

velocity. Noting that higher maximum internal velocity at critical point basically implies stronger inertia for droplets removal. Therefore, it can be concluded that proposed demister scheme with embedded drainage channels owns great potential for further improving separation performance and treating capability.

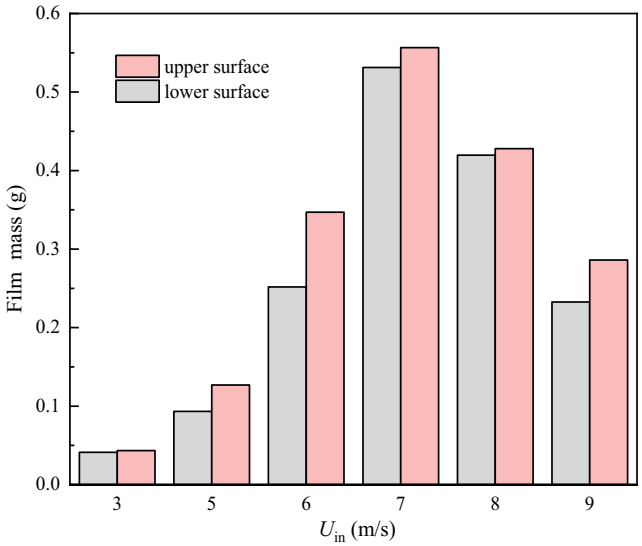

Fig. 20. Mass of liquid film attached on both sides of the plate.

4. Conclusions

An innovative type of demister that can be used in MSF facilities is proposed for the purpose of enhancing anti-re-entrainment ability and hence improving treating capability. The specific design is with embedded drainage channels integrated into the plates. Experimental and computational works are carried out to investigate the overall performance as well as the flow field details of the demister, key conclusions are:

Liquid film breakup is the dominant cause of re-entrainment in inertial demister, which is more significant than phenomena like droplets breakup and splash. Strong anti-re-entrainment ability is characterized by higher critical velocity which can be improved to 8.5 m/s with the proposed design. However, anti-re-entrainment performance must be trade off with the overall separation efficiency, anyway, the new type demister owns a high level of overall performance considering for both pressure loss and efficiency, especially at higher inlet velocities thanks to its outstanding anti-re-entrainment ability. Therefore, production quality and energy efficiency of MSF facilities can both be improved by equipping the proposed demister. Moreover, the most important significance of the present

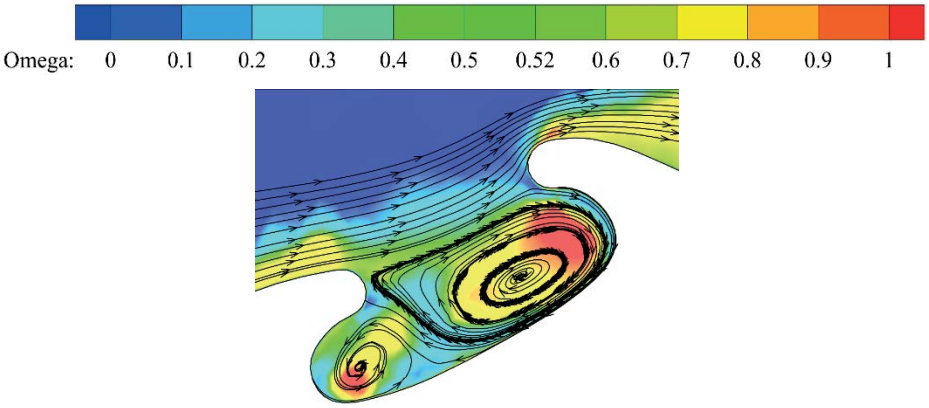

Fig. 21. Distribution of vortex intensity within embedded drainage channel.

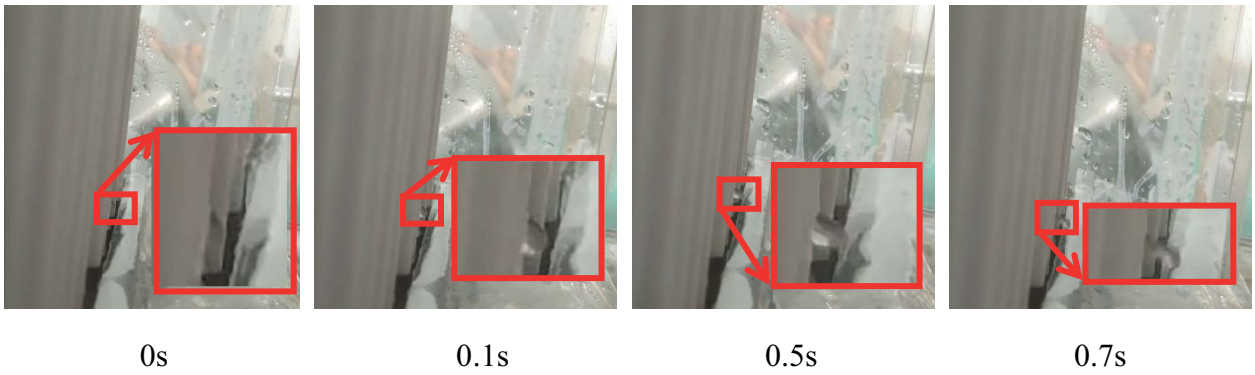

Fig. 22. Observation of re-entrainment in experiment.

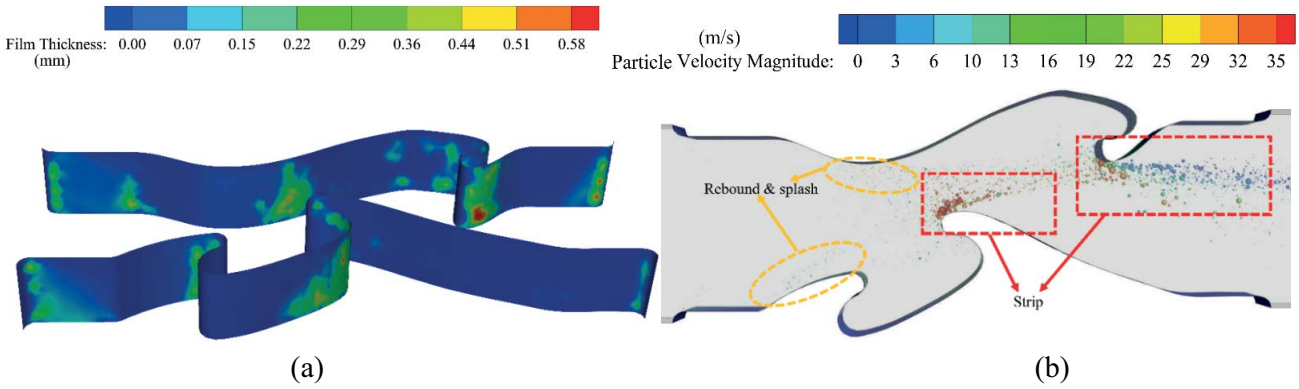

Fig. 23. Liquid film behavior: (a) distribution of film thickness and (b) creation of secondary droplets.

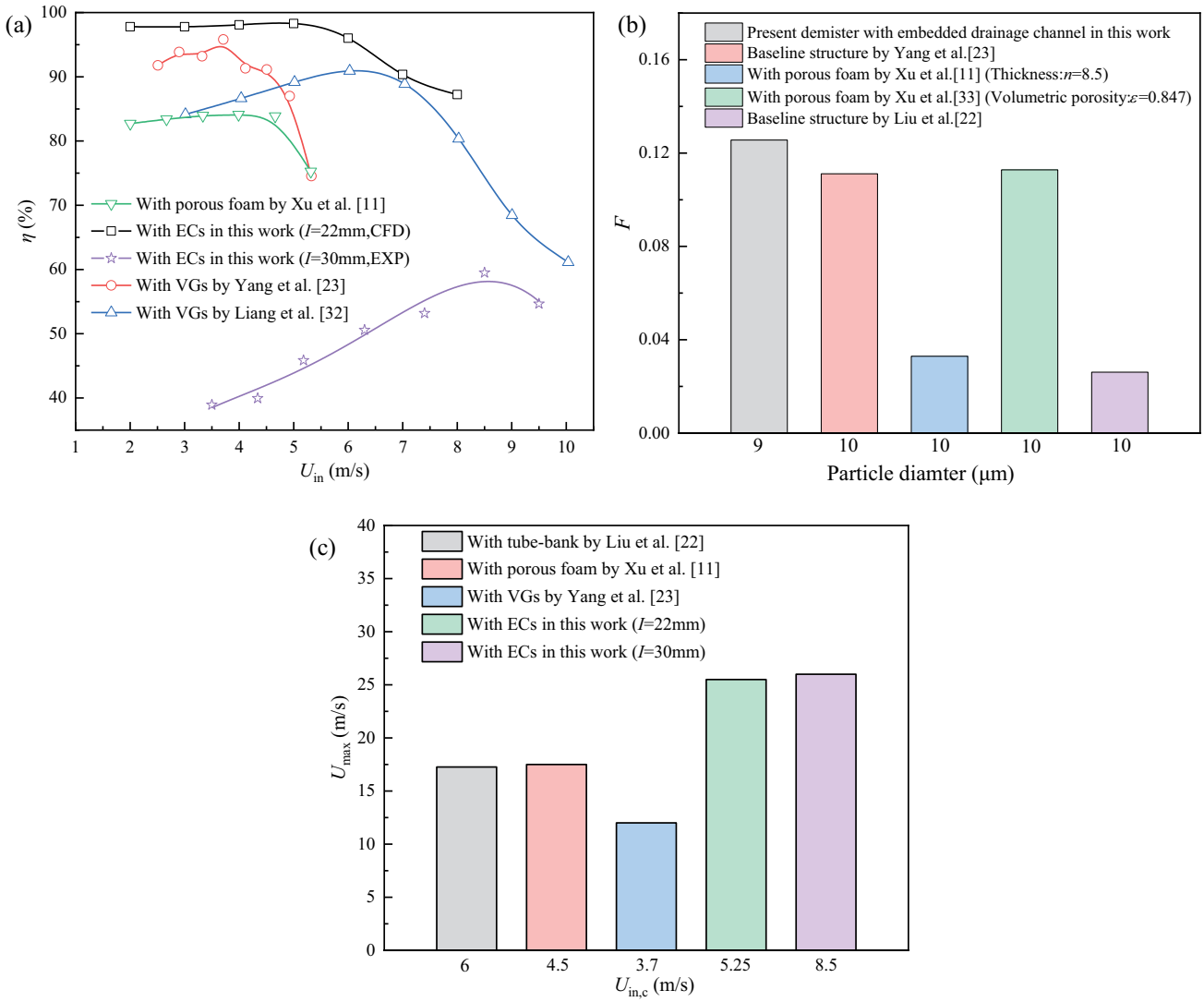

Fig. 24. Comparison of embedded drainage channel with conventional enhancing structures from literatures.

design lies in its potential of contributing to MSF system in achieving much higher treating capacity.

The adopted numerical method employing Euler-Wall-Film model successfully predicted the decrease of separation efficiency at higher inlet velocities due to droplets re-entrainment. It is found through numerical simulation that embedded drainage channels plays an ultra-important role in resisting secondary droplets by means of promoting film

spreading, suppressing shear force and creating vortex suction.

Apart from excellent anti-re-entrainment performance, the proposed demister scheme with embedded drainage channel is superior to conventional designs also due to the higher maximum internal velocity of 24–28 m/s at critical point, indicating great potential to further improve the overall performance through optimizing details of the embedded drainage channel.

Acknowledgments

This research is funded by National Natural Science Foundation of China (Funding No. 52201352) and Jiangsu Provincial Industry-University-Research Collaboration Project (Grant No. BY2022088). They are gratefully acknowledged.

Symbols

I	—	Plate interval, mm
h_1	—	Length of the front extension section, mm
h_2	—	Length of the rear extension section, mm
h_3	—	Length of the front deflector, mm
h_4	—	length of the rear deflector, mm
h_5	—	Length of the blade in the vertical direction, mm
H	—	Overall length of the plate, mm
$D(a/b)$	—	Structure ratio of the primary channel
L	—	Length of the third hook, mm
α	—	Angle of the third hook, °
Eu	—	Dimensionless Euler number
S	—	Length of the tip wall-normal direction, mm
P_{in}	—	Total pressure at the channel inlet, Pa
U_{max}	—	Maximum bulk flow velocity, m/s
U	—	Bulk flow velocity, m/s
U_{in}	—	Inlet velocity, m/s
$U_{in,c}$	—	Critical inlet velocity, m/s
ΔP	—	Pressure loss, Pa
P	—	The local total pressure, Pa
η	—	Separation efficiency, %
D_p	—	Droplet size, μm
F	—	Performance factor
δ	—	Film thickness, mm
τ_s	—	Wall shear stress, Pa

References

[1] S. Shaaban, Performance optimization of an integrated solar combined cycle power plant equipped with a brine circulation MSF desalination unit, Energy Convers. Manage., 198 (2019) 111794, doi: 10.1016/j.enconman.2019.111794.
[2] C.S. Bandi, R. Uppaluri, A. Kumar, Global optimization of MSF seawater desalination processes, Desalination, 394 (2016) 30–43.
[3] S. Lin, H. Zhao, L. Zhu, T. He, S. Chen, C. Gao, L. Zhang, Seawater desalination technology and engineering in China: a review, Desalination, 498 (2021) 114728, doi: 10.1016/j.desal.2020.114728.
[4] M. Ziyaei, M. Jalili, A. Chitsaz, M. Alhuyi Nazari, Dynamic simulation and life cycle cost analysis of a MSF desalination system driven by solar parabolic trough collectors using TRNSYS software: a comparative study in different world regions, Energy Convers. Manage., 243 (2021) 114412, doi: 10.1016/j.enconman.2021.114412.
[5] S. Kabiri, M.H. Khoshgoftar Manesh, M. Yazdi, M. Amidpour, New procedure for optimal solar repowering of thermal power plants and integration with MSF desalination based on environmental friendliness and economic benefit, Energy Convers. Manage., 240 (2021) 114247, doi: 10.1016/j.enconman.2021.114247.
[6] E. Jones, M. Qadir, M.T.H. van Vliet, V. Smakhtin, S.M. Kang, The state of desalination and brine production: a global outlook, Sci. Total Environ., 657 (2019) 1343–1356.
[7] Z.M. Ghazi, S.W.F. Rizvi, W.M. Shahid, A.M. Abdulhameed, H. Saleem, S.J. Zaidi, An overview of water desalination systems integrated with renewable energy sources, Desalination, 542 (2022) 116063, doi: 10.1016/j.desal.2022.116063.
[8] M. Ayaz, M.A. Namazi, M.A.u. Din, M.I.M. Ershath, A. Mansour, e.-H.M. Aggoune, Sustainable seawater desalination: current status, environmental implications and future expectations, Desalination, 540 (2022) 116022, doi: 10.1016/j.desal.2022.116022.
[9] N. Ghaffour, J. Bundschuh, H. Mahmoudi, M.F.A. Goosen, Renewable energy-driven desalination technologies: a comprehensive review on challenges and potential applications of integrated systems, Desalination, 356 (2015) 94–114.
[10] H. Al-Fulaij, A. Cipollina, H. Ettouney, D. Bogle, Simulation of stability and dynamics of multistage flash desalination, Desalination, 281 (2011) 404–412.
[11] Y. Xu, Z. Yang, J. Zhang, Study on performance of wave-plate mist eliminator with porous foam layer as enhanced structure. Part I: numerical simulation, Chem. Eng. Sci., 171 (2017) 650–661.
[12] R. Kouhikamali, S.M.A. Noori Rahim Abadi, M. Hassani, Numerical study of performance of wire mesh mist eliminator, Appl. Therm. Eng., 67 (2014) 214–222.
[13] J. Ruiz, C.G. Cutillas, A.S. Kaiser, B. Zamora, H. Sadafi, M. Lucas, Experimental study on pressure loss and collection efficiency of drift eliminators, Appl. Therm. Eng., 149 (2019) 94–104.
[14] E. Narimani, S. Shahhoseini, Optimization of vane mist eliminators, Appl. Therm. Eng., 31 (2011) 188–193.
[15] H.E.S. Fath, M.A. Ismail, An online cleaning system to reduce demister fouling in MSF Sidi Krir Desalination Plant, 2 × 5,000 m^3/day, Desalination, 220 (2008) 252–257.
[16] I. Janajreh, A. Hasania, H. Fath, Numerical simulation of vapor flow and pressure drop across the demister of MSF desalination plant, Energy Convers. Manage., 65 (2013) 793–800.
[17] C. Zhao, J. Zhao, M. Cong, H. Shen, Simulation study on the corrugated plate gas-liquid separator with the assistance of the drainage hook, ACS Omega, 7 (2022) 44134–44146.
[18] H. Lv, Y. Wang, L. Wu, Y. Hu, Numerical simulation and optimization of the flash chamber for multi-stage flash seawater desalination, Desalination, 465 (2019) 69–78.
[19] C. Fang, R. Zou, G. Luo, Q. Ji, R. Sun, H. Hu, X. Li, H. Yao, CFD simulation design and optimization of a novel zigzag wave-plate mist eliminator with perforated plate, Appl. Therm. Eng., 184 (2021) 116212, doi: 10.1016/j.applthermaleng.2020.116212.
[20] Z. Yu, C. Sun, J. Fang, L. Zhang, Y. Hu, B. Bao, S. Bu, W. Xu, Y. Ji, Water recovery efficiency improvement using the enhanced structure of the mist eliminator, Process. Saf. Environ., 154 (2021) 433–446.
[21] Y. Tang, Y. Xu, B. Zhang, C. He, Q. Chen, J. Ren, An integrated computational strategy for the geometric design and prioritization of wave-plate mist eliminators, Process. Saf. Environ., 158 (2022) 674–686.
[22] Y. Liu, D. Yu, J. Jiang, X. Yu, H. Yao, M. Xu, Experimental and numerical evaluation of the performance of a novel compound demister, Desalination, 409 (2017) 115–127.
[23] L. Yang, M. Xu, J. Wang, L. Song, J. Wang, Experimental and numerical analysis of a demister with vortex generators, Chin. J. Chem. Eng., 33 (2021) 83–95.
[24] H. Zhou, Y. Jin, L. Zhu, Z. Li, Numerical simulation of droplets re-entrainment in baffle demister, Part. Sci. Technol., 40 (2021) 567–575.
[25] S. Yuan, Y. Fan, H. Lin, Influence of discrete particle diameter and separating velocity on the separation efficiency of

wave-plate separator including coalescence and breakup model, J. Dispersion Sci. Technol., 37 (2015) 1324–1333.
[26] F. Mao, R. Tian, Y. Chen, B. Chen, B. Wang, L. Sun, Re-entrainment in and optimization of a vane mist eliminator, Ann. Nucl. Energy, 120 (2018) 656–665.
[27] R.J. Moffat, Describing the uncertainties in experimental results, Exp. Therm. Fluid Sci., 1 (1988) 3–17.
[28] Y. Luan, S. Bu, H. Sun, T. Sun, Numerical Investigation on Flow and Heat Transfer in Matrix Cooling Channels for Turbine Blades, ASME Turbo Expo 2016: Turbomachinery Technical Conference and Exposition, Seoul, South Korea, 2016. Available at: https://doi.org/10.1115/GT2016-56279
[29] P.J. O'Rourke, Collective Drop Effects on Vaporizing Liquid Sprays, Ph.D. Thesis, Princeton University, Princeton, NJ, USA, 1981. Available at: www.osti.gov/biblio/5201366-collective-drop-effects-vaporizing-liquid-sprays (Last Accessed on October 30th, 2022).
[30] S. Yuan, Y. Fan, B. Chen, J. Li, L. Gao, S. Zhang, Forming and stripping of the wall film and the influence on gas–liquid separation, Asia-Pac. J. Chem. Eng., 15 (2020) e2447, doi: 10.1002/apj.2447.
[31] C. Liu, Y. Wang, Y. Yang, Z. Duan, New omega vortex identification method, Sci. China Phys. Mech., 59 (2016) 1–9.
[32] H. Liang, H. Song, X. Jiang, C. Li, J. Ma, Study on the performance of a vortex mist eliminator for improving the separation efficiency of fine particles, Asia-Pac. J. Chem. Eng., 17 (2022) e2757, doi: 10.1002/apj.2757.
[33] Y. Xu, Z. Yang, J. Zhang, Study on performance of wave-plate mist eliminator with porous foam layer as enhanced structure. Part II: experiments, Chem. Eng. Sci., 171 (2017) 662–671.